Highly Stable and Efficient Light-Emitting Diodes Based on Orthorhombic γ-$CsPbI_3$ Nanocrystals

Guo, Jie; Lu, Min; Zhang, Xiaoyu; Sun, Siqi; Han, Ce; Zhang, Yu; Yang, Xuyong; V. Kershaw, Stephen; Zheng, Weitao; Rogach, Andrey L.

Published in:
ACS Nano

Published: 23/05/2023

Document Version:
Post-print, also known as Accepted Author Manuscript, Peer-reviewed or Author Final version

Published version (DOI):
10.1021/acsnano.3c00789

Publication details:
Guo, J., Lu, M., Zhang, X., Sun, S., Han, C., Zhang, Y., Yang, X., V. Kershaw, S., Zheng, W., & Rogach, A. L. (2023). Highly Stable and Efficient Light-Emitting Diodes Based on Orthorhombic γ-$CsPbI_3$ Nanocrystals. *ACS Nano*, *17*(10), 9290-9301. https://doi.org/10.1021/acsnano.3c00789

Highly stable and efficient light-emitting diodes based on orthorhombic γ-$CsPbI_3$ nanocrystals

Jie Guo[#], Min Lu[#], Xiaoyu Zhang*, Siqi Sun, Ce Han, Yu Zhang*, Xuyong Yang, Stephen V. Kershaw, Weitao Zheng*, and Andrey L. Rogach*

Abstract

Orthorhombic γ-$CsPbI_3$ possesses the highest structural stability among the optically active (light-emissive) $CsPbI_3$ perovskites. Here, we make use of a seed-assisted heteroepitaxial growth to fabricate seed/core/shell CaI_x/γ-$CsPbI_3$/CaI_2 nanocrystals. Ultrasmall CaI_x nanoparticles serve as seeds to template the Pb-centered octahedral arrangement which enables the formation of the γ-$CsPbI_3$ phase, and at the same time inhibit lattice strain by blocking the force transfer that otherwise leads to octahedral twist and so improve the structural stability of the resulting nanocrystals. An outer shell composed from the same material, CaI_2, isolates the formed γ-$CsPbI_3$ nanocrystals from the environment, which also significantly improves their stability under ambient conditions. Optical and electrical studies indicate that the seed/core/shell CaI_x/γ-$CsPbI_3$/CaI_2 structure possesses a shallower set of trap states as compared to cubic α-$CsPbI_3$ nanocrystals. Light-emitting diodes utilizing these γ-$CsPbI_3$ nanocrystals show a record high external quantum efficiency of 25.3%, high brightness of over 13,600 cd/m^2, and an operational lifetime of ~14 h before reaching 50% of their initial luminance. These devices can repeatedly be illuminated over 650 times at ~500 cd/m^2 with no decline of brightness, which indicates their great commercial potential.

Keywords: Orthorhombic γ-$CsPbI_3$ phase; seed/core/shell nanostructure; light-emitting diode; CaI_2 nanoparticles; stable light-emitting devices

Introduction

The bright and narrow-band light emission of perovskite nanocrystals (NCs) which is tunable across the visible and near-infrared spectral range enables fabrication of efficient light-emitting diodes (LEDs) with pure colors.[1-4] Perovskite can be engineered both compositionally and structurally to manipulate and adjust their optical and electronic properties.[5-7] All-inorganic $CsPbI_3$ NCs which combine attractive thermal stability with solution processability have emerged as novel emitters for stable and cost-effective deep-red LEDs for a wide range of applications in biomedical imaging, photodynamic therapy, and optical communications.[8-11] Optically active (light-emitting) $CsPbI_3$ perovskites can belong to the following three structural phases: cubic α-, tetragonal β-, and orthorhombic γ-$CsPbI_3$; all these phases are so-called *black phases*, whereas transition between them is governed by the local Pb-centered $[PbI_6]^{4-}$ octahedral distortions. Among the black phases, γ-$CsPbI_3$ is the most stable,[12, 13] because its tolerance factor calculated using radii of Cs^+, Pb^{2+}, and I^- ions satisfies the most desired range for stable orthorhombic phase (0.805 ± 0.095),[13] and it also has the lowest surface free energy and thus the highest thermodynamic stability.[14, 15] For the perovskite nanocrystals, it has been demonstrated by theoretical calculations combined with experiments that γ-$CsPbI_3$ phase with a lower surface free energy becomes thermodynamically preferred over δ-$CsPbI_3$. The disparity in the surface energy between γ-$CsPbI_3$ (0.13 J/m^2) and δ-$CsPbI_3$ (2.57 J/m^2) leads to a reversal in the relative magnitudes of their Gibbs free energies at surface areas larger than ~8600 m^2/mol, which changes their relative phase stability.[16] The surface area of typical perovskite

NCs with a size of ~10 nm is larger than that, so that their γ-phase is more stable. However, experimentally the direct formation of γ-$CsPbI_3$ phase NCs is difficult because of the uncontrollable crystallization kinetics,[17] mainly due to the difficulty in controlling the arrangement of the Pb-centered octahedral units, which typically leads to the formation of cubic α-$CsPbI_3$ NCs instead. Although plenty of strategies including ligand engineering,[18-20] ion doping,[21-23] and epitaxial shell growth[24, 25] have been proposed to stabilize the crystal structure of α-$CsPbI_3$ NCs, in respect to phase stability, $CsPbI_3$ perovskite can readily transform into a yellow δ-phase (non-perovskite phase) under ambient conditions.[16, 26, 27] This arises from the inherent structural property of the initial black phase $CsPbI_3$ perovskite with a low value of tolerance factor (0.81).[12, 28] Also loss of surface ligands during the purification process can causes NC agglomeration[29, 30] which greatly accelerates the formation of undesired yellow δ-$CsPbI_3$ phase. This limitation represents an impediment for the use of $CsPbI_3$ NCs in fabrication of high-performance LEDs.

In this study, taking advantage of the mentioned phase stability of γ-$CsPbI_3$, we have established a seed-assisted heteroepitaxial growth strategy, which enables the growth of γ-$CsPbI_3$ starting from ultrasmall CaI_x nanoparticles as seeds (see **Figure S1**). At the same time, CaI_2 nanoparticles are spontaneously adsorbed on the outside of CaI_x/γ-$CsPbI_3$ NCs thus forming seed/core/shell nanostructures, which passivates the iodine vacancy defects of the NC cores and isolates them from the ambient environment, enabling bright and stable seed/core/shell CaI_x/γ-$CsPbI_3$/CaI_2 NCs with high photoluminescence (PL) quantum yields (PL QY) ranging from 55% to over 90%,

alongside with rather narrow full width at half maximum (FWHM) of their PL peak equal to 31 nm, and over 100-times enhanced stability when compared to α-$CsPbI_3$ NCs. Electroluminescent LEDs employing these γ-$CsPbI_3$ NCs show significant improvements in external quantum efficiency (EQE: 25.3%) and brightness (13,626 cd/m^2); they reach operational stability of about 14 h and can repeatedly be illuminated over 650 times at ~500 cd/m^2 with no decline of brightness.

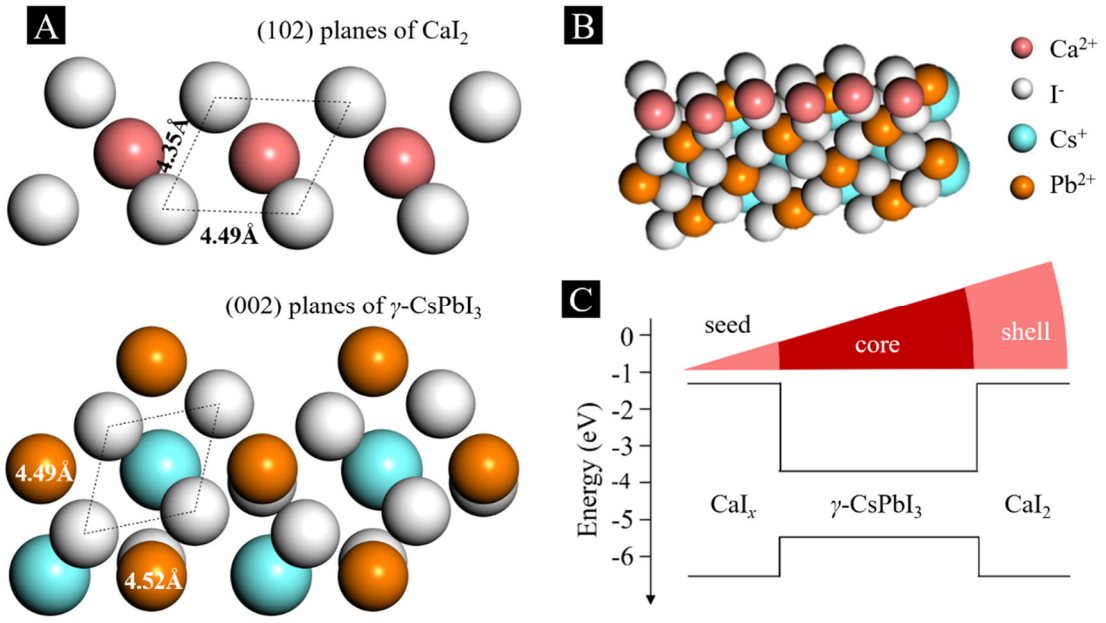

Figure. 1. Crystal structure and electronic structure of seed/core/shell CaI_x/γ-$CsPbI_3$/CaI_2 NCs. (**A**) The unit cell structure of the (102) planes of CaI_2 (upper part) and the (002) planes of γ-$CsPbI_3$ (bottom part). (**B**) Crystal structure of an epitaxial heterojunction between CaI_2 and γ-$CsPbI_3$. (**C**) Energy level diagram of the seed/core/shell CaI_x/γ-$CsPbI_3$/CaI_2 NCs.

Results

Formation of seed/core/shell CaI_x/γ-$CsPbI_3$/CaI_2 NCs. According to the interplanar crystal spacing of CaI_2 and γ-$CsPbI_3$ illustrated in **Figure 1A**, the (102) planes of CaI_2 and the (002) planes of γ-$CsPbI_3$ should match each other with a high matching degree

of over 96%. From the standard X-ray diffraction (XRD) patterns of CaI_2 (ICSD: 4481) and γ-$CsPbI_3$ (ICSD: 264725) provided in **Figure S2A** and the interplanar crystal spacing and crystal planes of the CaI_2 and γ-$CsPbI_3$ corresponding to different XRD peaks (**Table S1**), we can see that there is a good lattice match between these two materials. Thus, such a slight lattice mismatch (4%) can allow for the epitaxial growth of γ-$CsPbI_3$ rather than of the α-$CsPbI_3$ phase on top of CaI_2, as shown in **Figure 1B**. Exposed (102) planes of CaI_2 nanoparticles can allow them to act as 'seeds' where Pb-centered octahedral units and precursor ions react, thus enabling the heteroepitaxial growth of γ-$CsPbI_3$.

CaI_x seeds were obtained by quenching the reaction before injecting Cs-OA precursors, resulting in a crude solution containing ODE, PbI_x, CaI_x, OA, and OLA. When $R_{<Ca/Pb>}$ was 0.25, the solution was clear and transparent. When $R_{<Ca/Pb>}$ increased to 0.5, the solution became a suspension, indicating formation of colloidal particles, which were separated by centrifugation at 10000 rpm for 10 min, and re-dispersed in toluene for TEM study. The TEM image in **Figure S3A** shows the existence of CaI_x nanoparticles around 3 nm in size, whose HRTEM image provided in inset shows a lattice spacing of 2.6 Å which is consistent with the (102) planes of CaI_2. Using EDS characterization (**Figure S3B and C**), we found that the Ca element was present in a high proportion, namely the atomic percent Ca/(Ca+Pb) was estimated to be 88.4%, which is indicative of the CaI_x seed formation.

We also conducted control experiments to demonstrate that the γ-$CsPbI_3$ formation depends on the presense of suitable seeds; this was realized by choosing seeds with

better lattice matching and thus weaker stress to template the growth of $CsPbI_3$ NCs. Specifically, PbS nanoparticles were employed as seeds, because the lattice mismatch between their (200) and γ-$CsPbI_3$ (100) planes is about 3%, slightly higher than 2% latttice mismatch between CaI_x (**Figure S4A and B**) and α-$CsPbI_3$ but lower than 4% of that between CaI_x and γ-$CsPbI_3$.[1] From the XRD pattern (**Figure S4C**), $CsPbI_3$ NCs synthesized with PbS nanoparticles as seeds belong to the cubic phase. Thus, the use of CaI_x seeds is necessary to induce the formation of γ-$CsPbI_3$ NCs.

We further considered the feasibility of this 'seed-assisted heteroepitaxial growth strategy' from the energy point of view. We calculated the values of the ion energy of Pb^{2+} and Ca^{2+}, the system energy of lead-oleic acid (OA) and calcium-OA, and the binding energy of Pb-Oleate (Pb-OA_2) and Ca-Oleate (Ca-OA_2) (see **Table S2**), and found out that all these energies for Pb and Ca are quite close to each other (**Figure S2B**). Since the ligands are essential for the stability and electrical properties of NCs, such similarity in energies also suggests that there would be little to no ligand competition between the highly dynamic metal oleates (Pb-OA_2 and Ca-OA_2) during the synthesis, meaning that the rate of NC formation would remain the same and the surface ligand density would not be significantly changed.[31, 32] This in turn indicates that the introduction of Ca^{2+} ions as a precursor can easily lead to the formation of doped-, alloyed-perovskite NCs, or CaI_x NCs, depending on the existent form of the Ca^{2+} ions. There are three types of ligands on colloidal NCs: X-type, L-type, and Z-type [need some reference here], and the ligands of ionic perovskite NCs belong to X-type. OLA cations bind to surface halide atoms via hydrogen bonds, whereas halide

anions and carboxylates coordinate with cations on the surface.[31] As a result of the ionic nature and low formation energy of perovskites, these ligands tend to desorb/adsorb rapidly, reaching a dynamic equilibrium.[31, 51] As a result, lead halide perovskites are referred to as having 'highly dynamic' surface ligands.[52, 53]

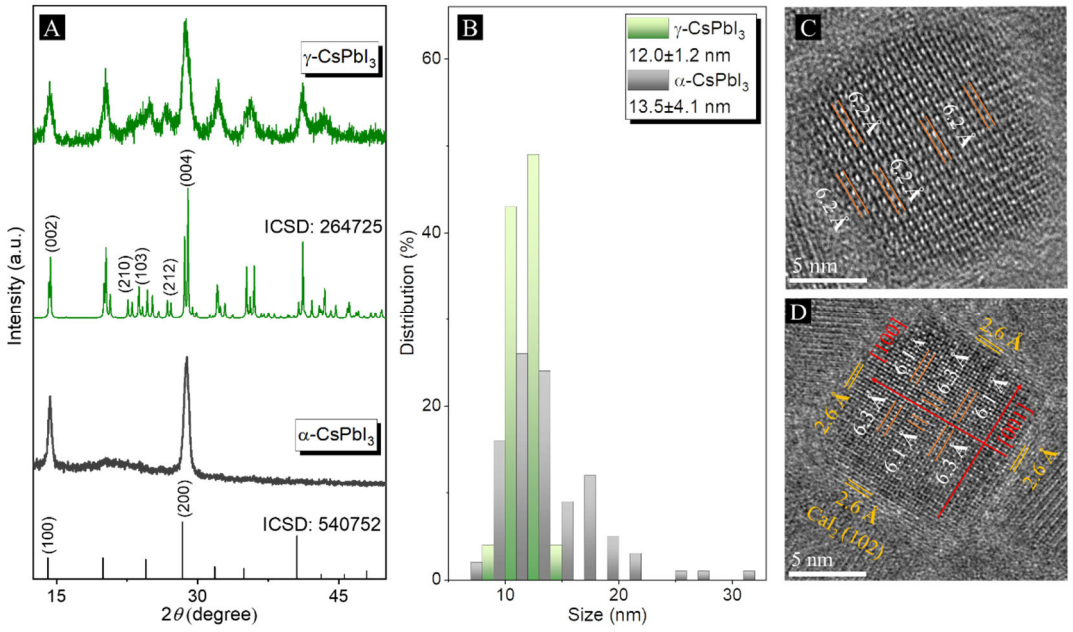

Figure. 2. Structure and morphology characterization of *α*- and *γ*-CsPbI$_3$ NCs. (**A**) Experimental XRD patterns of *α*-CsPbI$_3$ (gray line, ICSD: 540752) and *γ*-CsPbI$_3$ NCs (green line, ICSD: 264725) films on quartz substrate. (**B**) The particle size distribution histograms obtained using the TEM images of Figure S5. (**C** and **D**) HRTEM images respectively of *α*-CsPbI$_3$ (6.2 Å) of (100) interplanar distances, *γ*-CsPbI$_3$ NCs (6.1 or 6.3 Å) of (002) interplanar distances and CaI$_2$ NCs of (102) interplanar distances 2.6 Å.

CsPbI$_3$ perovskite NCs were synthesized as outlined in detail in the Methods Section, by injecting Cs-OA into the precursor mixture containing M-OA (M = Pb, Ca) and iodine oleylamine (OLA) at temperatures ranging from 150 to 170 °C. The key to determine the formation of *γ*-CsPbI$_3$ NCs or the common *α*-phase CsPb$_y$Ca$_{1-y}$I$_3$ ($0 < y \leqslant 1$) NCs appears to be the feeding ratio of the CaI$_2$ and PbI$_2$ precursors ($R_{<Ca/Pb>}$)

before Cs-OA injection, which varied between 0, 0.25, 0.5, and 0.75. When the $R_{<Ca/Pb>}$ was smaller than 0.25, the M-OA containing precursor was completely clear and transparent; when the $R_{<Ca/Pb>}$ was around 0.5, the M-OA containing precursor turned into a colloidal solution containing CaI_2 nanoparticles; when the $R_{<Ca/Pb>}$ was increased to 0.75, turbid precipitates appeared in the M-OA containing precursor (**Figure S5**). On one hand, the CaI_2 nanoparticles can act as seeds and enable the heteroepitaxial growth of γ-$CsPbI_3$. On the other hand, those CaI_2 nanoparticles which are not serving as growth centers can be adsorbed on to the surface of γ-$CsPbI_3$ NCs forming CaI_x/γ-$CsPbI_3/CaI_2$ seed/core/shell NCs. As a result, α-phase $CsPb_yCa_{1-y}I_3$ ($0<y\leqslant 1$) NCs were obtained when the $R_{<Ca/Pb>}$ was less than 0.25, while CaI_x/γ-$CsPbI_3/CaI_2$ NCs were obtained when the $R_{<Ca/Pb>}$ more than 0.5, as evidenced by the XRD pattens in **Figure 2A** and **Figure S6**.

Transmission electron microscopy (TEM) was performed to characterize the structure of the α-$CsPbI_3$ NCs, and the γ-$CsPbI_3$ NCs obtained with $R_{<Ca/Pb>} = 0.5$. As shown in **Figure S7**, the shape of the particles in both cases is square-like, and the size distribution of the γ-$CsPbI_3$ NCs is obviously narrower than that of the α-$CsPbI_3$ NCs. The average particle sizes of α-$CsPbI_3$ and γ-$CsPbI_3$ NCs are 13.5 ± 4.1 and 12.0 ± 1.2 nm, respectively (**Figure 2B**). High resolution TEM (HRTEM) images shown in **Figure 2C and 2D** highlight that both perovskite NCs possess well-defined crystalline structures, consistent with the XRD data. For α-$CsPbI_3$ NCs, interplanar distances of 6.2 Å corresponding to (100) crystal facets are identified. For γ-$CsPbI_3$ NCs, some of the interplanar distances are wider and some are narrower than 6.2 Å rather than being

fixed to a constant value, which may be the result of the crystal structure distortion caused by $[PbI_6]^{4-}$ octahedral rearrangement templated by the CaI_x seeds. **Figure S8B** shows the fast Fourier transformed (FFT) pattern of a γ-$CsPbI_3$ NC. Interplanar distances of 6.2 Å which appear in the FFT pattern belong to (002) planes. Importantly, there are obvious bright spots on the inside and outside of the (002) plane as emphasized by blue circles, which are consistent with 6.1 and 6.3 Å interplanar distances, demonstrating that the NC belongs to the γ-phase. Besides, the presence of the CaI_2 shell at the surface of γ-$CsPbI_3$ NC is observed, whose interplanar distances are measured as 2.6 Å which corresponds to the (102) facets of CaI_2. The elemental mapping and EDX analysis (**Figure S9**) show the distribution of Cs, Pb, Ca, and I elements over the γ-$CsPbI_3$ NCs, demonstrating the presence of Ca all over the structures.

To identify the differences in the structure and chemical states between α-$CsPbI_3$ and γ-$CsPbI_3$ NCs, X-ray photoelectron spectroscopy (XPS) measurements were conducted. **Figure S10** shows high-resolution XPS spectra of Cs 3d, Pb 4f, and I 3d for α-$CsPbI_3$ and γ-$CsPbI_3$ NCs, all calibrated with C 1s. The Cs 3d, Pb 4f, and I 3d peaks of γ-$CsPbI_3$ NCs all shift to lower binding energies compared to those peaks of α-$CsPbI_3$ NCs, which is opposite to the effect caused by B-site ion doping[21, 22] but coincides with the phase transition from α to γ.[33] Besides, α-$CsPbI_3$ NCs show two more small peaks at 136.9 and 141.6 eV when compared with γ-$CsPbI_3$, which belong to metallic Pb.[34, 35] The absence of metallic Pb in γ-$CsPbI_3$ NCs is beneficial for efficient radiative recombination.[31] Thus, XPS data further illustrate the role of CaI_x nanoparticles which

serve as the template for perovskite growth and at the same time are helpful to passivate surface defects when deposited as shell.

The presence of the CaI_2 shell on the surface of γ-$CsPbI_3$ NCs has been further confirmed by comparing the high-resolution XPS spectra of Ca 2p of γ-$CsPbI_3$ NCs from different purification cycles. Due to the highly ionic nature of $CsPbI_3$, thorough purification of the NCs by adding ethyl acetate can induce the equilibrium between reconstruction of the NC surface. As shown in **Figure. S11A** in Supporting Information, Ca 2p peaks can be easily detected from γ-$CsPbI_3$ NCs when purified once,[28, 36] but they disappeared when the NCs were twice purified, indicating the removal of surface CaI_2 components. The Cs 3d, Pb 4f, and I 3d peaks did not change after secondary centrifugation, but Pb 4f and I 3d peaks became slightly broader, possibly due to the removal of CaI_2 from the surface. The unchanged positions of the XPS peaks further confirm the seed-induced improvement of the structural stability of the γ phase of perovskite NCs.

Spectroscopic study of perovskite NCs. In the CaI_x/γ-$CsPbI_3$/CaI_2 NCs, both the CaI_x seed and the CaI_2 shell have a larger bandgap than the interior γ-$CsPbI_3$ region (see **Figure 1C**), enabling the preferential location of both electrons and holes in the perovskite emitter region, which should be beneficial for the radiative recombination processes in these seed/core/shell NCs. Absorption and PL spectra of $CsPbI_3$ NCs with different $R_{<Ca/Pb>}$ are provided in **Figure S12**, which appear as typical spectra of conventional perovskite NCs. The PL peak experiences a blue-shift from 691 to 684 nm as the $R_{<Ca/Pb>}$ increases from 0 to 0.75, which is size dependent. The average

particle sizes of the samples with $R_{<Ca/Pb>}$ = 0, 0.25, 0.5, and 0.75 are 13.5 ± 4.1, 12.7± 1.9, 12.0 ± 1.2, and 9.5 ± 1.0 nm, respectively, as shown in **Figure S13**. At the same time, the absolute PL QY increases from 55% to 98% (**Figure 3A**). The γ-$CsPbI_3$ NCs produced with $R_{<Ca/Pb>}$ = 0.5 have the narrowest full-width at half-maximum (FWHM) of their PL peak equal to 31 nm, and the highest PL QY among all samples (98%), and thus they were chosen for further optical studies and for the fabrication of LEDs.

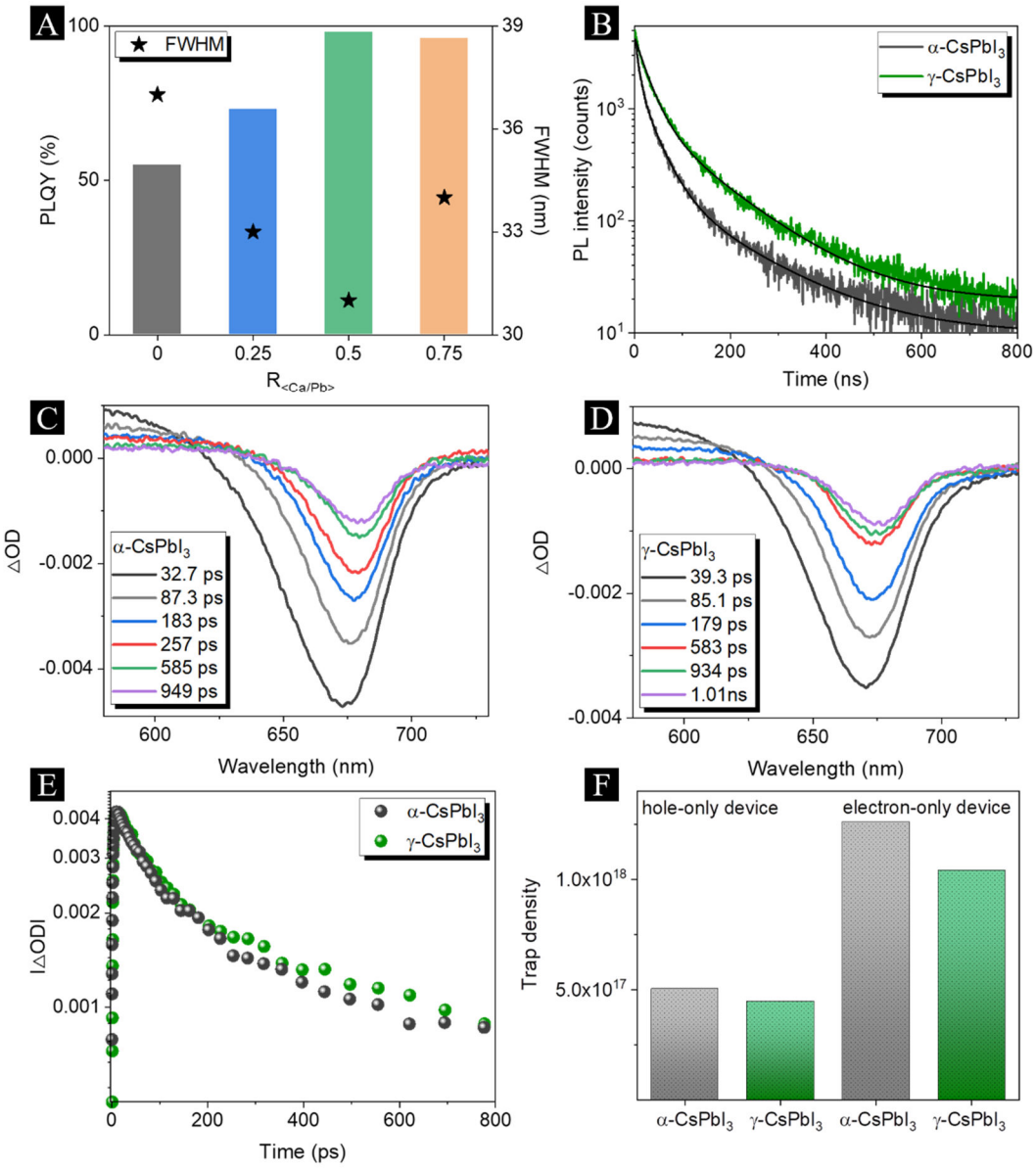

Figure. 3. Carrier dynamics studies of α-$CsPbI_3$ and γ-$CsPbI_3$ NCs. (**A**) PL QYs and FWHM of $CsPbI_3$ produced using different values of $R_{<Ca/Pb>}$. (**B**) TRPL decays of α-

$CsPbI_3$ and γ-$CsPbI_3$ NCs. (**C**) TA spectra of α-$CsPbI_3$ NCs and (**D**) γ-$CsPbI_3$ NCs, recorded at different pump-probe decay times with an excitation wavelength of 390 nm. (**E**) TA spectra comparisons of bleach recovery kinetics monitored at ~ 672 nm for α-$CsPbI_3$ (gray line) and γ-$CsPbI_3$ NCs (green line). (**F**) Trap densities obtained from the dark current-voltage measurements of the hole-only and electron-only devices. The hole-only device structure is ITO/PEDOT:PSS/perovskite/MoO_x/Ag, and the electron-only device structure is ITO/ZnO/PEI/perovskite/LiF/Al. Thicknesses of the PEDOT:PSS, perovskite and ZnO/PEI films are ~30 nm; thicknesses of the Ag and Al electrodes are ~100 nm; thicknesses of the MoO_x and LiF layers are ~1 nm.

Time-resolved PL (TRPL) spectroscopy was carried out on α-$CsPbI_3$ and γ-$CsPbI_3$ NCs. As can be seen from **Figure 3B**, the PL average lifetime (determined from bi-exponential fitting) increases from 56.2 ns to 79.3 ns on transition from α-$CsPbI_3$ to γ-$CsPbI_3$ (see **Table S3**). Given the corresponding increase of PL QY from 55% to 98% for these two materials, we have calculated the radiative (k_r) and apparent nonradiative (k_{nr}) recombination rates,[1, 21, 37] which are summarized in **Table S4**. Here we use the term 'apparent' because the simply calculated non-radiative lifetime and recombination rates do not take into account the influence of any dark fraction of emitters and changes in this fraction that may occur alongside changes in the true non-radiative factors**.** Upon the phase change from cubic (α-$CsPbI_3$) to orthorhombic (γ-$CsPbI_3$) NCs, k_r increases from 9.8×10^6 s^{-1} to 12.4×10^6 s^{-1}, whilst the apparent k_{nr} decreases from 8.0×10^6 s^{-1} to 0.3×10^6 s^{-1}, with most of this difference stemming from the much lower PL QY, indicating that the trap states have been better passivated in the γ-$CsPbI_3$ structure.

Transient absorption (TA) spectra shown in **Figure 3C and 3D** reveal how the

dynamics of photogenerated carriers is influenced within the γ-$CsPbI_3$ NCs. The optical density (ΔOD) change detected by TA spectroscopy is proportional to the exciton density in the lowest excited state. After excitation, the photoexcited carriers relax to the lowest-energy sites before emitting photons, which appears as a redshift of the transient bleach minimum relative to the energy states distribution. The transient bleach peak of α-$CsPbI_3$ NCs is redshifted by ~ 7 nm (from 673 to 680 nm) (**Figure 3C**), while that of γ-$CsPbI_3$ NCs is redshifted by ~ 3 nm (from 671 to 674 nm) (**Figure 3D**). In addition, the bleach recovery dynamics are much slower for the γ-$CsPbI_3$ NCs (**Figure 3E**), indicating slower elimination of excitons. The reduced redshift in the transient bleach and the slowed bleach recovery dynamics are consistent with the narrowed PL FWHM and improved PL QY, indicating that a more homogeneous and shallower energy level distribution for charges is realized in the γ-$CsPbI_3$ NCs.[38] This has been further confirmed by current-voltage characterizations performed on a series of hole-only and electron-only devices. The hole-only devices had a structure of ITO/PEDOT:PSS/NCs/MoO_x/Ag, and the electron-only devices had a structure of ITO/ZnO/PEI/NCs/LiF/Al, where PEDOT:PSS is poly(3,4-ethylenedioxythiophene):poly(styrenesulfonate) and PEI is polyethylenimine. Trap density (N_t) and charge carrier mobilities (μ) determined from the dark current-voltage characterization of hole-only and electron-only devices are provided in **Figure S14**. Derived from those measurements[39, 40] and summarized in **Figure 3F**, the hole trap density decreases from 5.03×10^{17} to 4.46×10^{17} cm^{-3}, and the electron trap density decreases from 1.26×10^{18} to 1.04×10^{18} cm^{-3} along with the phase transformation from

α-$CsPbI_3$ to γ-$CsPbI_3$.

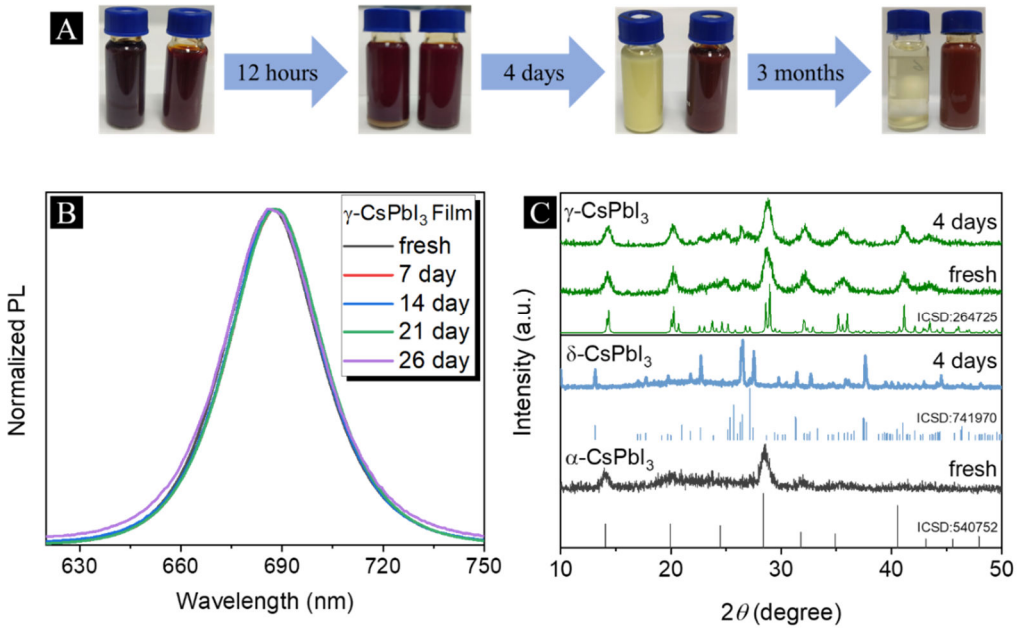

Figure 4. (**A**) A series of photographs showing the change in appearance of colloidal solutions of α-$CsPbI_3$ (left) and γ-$CsPbI_3$ NCs (right) during their storage in air for 12 h, 4 days and 3 months. (**B**) PL spectra of γ-$CsPbI_3$ NC films monitored for up to 26 days. (**C**) XRD patterns of the films of γ-$CsPbI_3$ (upper part) and α-$CsPbI_3$ (bottom part) NCs, measured as freshly made samples (black curves) and those stored in air for 4 days (blue curves, δ-phase). The γ-$CsPbI_3$ retained their orthorhombic phase, while α-$CsPbI_3$ NCs converted into a non-perovskite δ-phase.

Stability of α-$CsPbI_3$ and γ-$CsPbI_3$ NCs. The perovskite stability can be affected by both the crystal structure of the lattice and the presence of defects. Given that γ-$CsPbI_3$ NCs produced in this work are not only a more stable phase but also have reduced trap densities, we expect them to show a much improved stability as compared to α-$CsPbI_3$ NCs. Indeed, as can be seen from photographs shown in **Figure 4A**, the appearance of colloidal solutions of γ-$CsPbI_3$ NCs in toluene does not change for over 3 months storage in air, while α-$CsPbI_3$ NCs in toluene undergo a phase transition to a

non-perovskite yellow δ-phase, which occurs already after 4 days of storage in air (in **Figure 4A left**, the solution has completely turned yellow). Monitoring the PL spectra of γ-$CsPbI_3$ NC films which were directly exposed to air further confirmed the excellent stability of these γ-$CsPbI_3$ NCs. As shown in **Figure 4B**, there was a negligible change of the PL spectra of γ-$CsPbI_3$ NC films monitored for up to 26 days, while the PL signal of α-$CsPbI_3$ NC films stored under the same conditions was completely quenched within only 2 days. We have also examined the phase stability of γ-$CsPbI_3$ NCs in air by monitoring their XRD patterns. As can be seen from **Figure 4C**, after 4 days of storage α-$CsPbI_3$ NCs fully converted into non-perovskite δ-phase, while γ-$CsPbI_3$ NCs retained their orthorhombic phase. At the same time, the electric field can drive ion migration, resulting in decomposition of perovskite emitters. Therefore, the material and structural stability of α-$CsPbI_3$ and γ-$CsPbI_3$ NCs can be verified, as shown in **Figure S15**. Capacitor-like devices (C-devices) were fabricated with NC films sandwiched between ITO/PEDOT:PSS and LiF/Al layers, as shown in **Figure S15A**. **Figure S15B** shows photographs of C-devices with α-$CsPbI_3$ NCs operated under a constant bias of 10 V bias, whose emitting zone becomes transparent and the metal electrode could be seen directly from the substrate side after 0.5 h. The emitter areas become dark which contrasts with the areas without electrodes, which is the result of performance degradation caused by Al atoms diffused from the metal electrodes,[2-5] indicating that α-$CsPbI_3$ NCs are rather unstable. In contrast, γ-$CsPbI_3$ NCs still shine brightly under the same driving voltage of 10 V, as illustrated in **Figure S15C**, demonstrating negligible changes even after 3 h and becoming slightly darker after 4 h.

These experiments provide additional demonstration that the structural stability of γ-$CsPbI_3$ NCs is higher than that of α-$CsPbI_3$ NCs in realtion to light-emitting device operation conditions.

Electroluminescence performances of α-$CsPbI_3$ and γ-$CsPbI_3$ NCs. Before examining the electroluminescence (EL) performance of perovskite emitters, absolute positions of the energy level of α-$CsPbI_3$ and γ-$CsPbI_3$ NCs were determined using ultraviolet photoelectron spectroscopy (UPS). **Figure S16A** presents UPS spectra for cutoff (left) and valence (right) regions, while **Figure S16B** shows Tauc plots for α-$CsPbI_3$ and γ-$CsPbI_3$ NC films, from which optical bandgaps equal to 1.78 eV and 1.79 eV, respectively have been obtained. Based on these data, the valence band maximum (VBM) derived for α-$CsPbI_3$ NCs is at -5.74 eV, and its Fermi level (-4.0 eV) and conduction band minimum (CBM, -3.96 eV) are close to each other, clearly identifying their *n*-type behavior. For CaI_x/γ-$CsPbI_3$/CaI_2 NCs, the CBM and VBM locate at -3.71 and -5.50 eV, respectively, and the Fermi level is around -4.3 eV, demonstrating their ambipolar behavior. Such a nearly ambipolar behavior of γ-$CsPbI_3$ NCs allows the fabrication of *p-i-n* structured LEDs, which are known for efficient tunnel injection and flat band conditions under operation. LEDs with the structure of ITO/ZnO/PEI/NCs/TCTA/MoO_x/Ag were fabricated (ITO is indium tin oxide), with the energy band diagram for all functional layers given in **Figure 5A**. A *p*-type 4,4,4″-tris(carbazol9yl)triphenylamine (TCTA) film was used as a hole transport layer (HTL), whose suitable highest occupied molecular orbital (HOMO) enables efficient hole injection, while the lowest unoccupied molecular orbital (LUMO) enables efficient

electron-blocking. A *n*-type ZnO NC film was used as an electron transport layer (ETL), whose wide bandgap ensures its excellent optical transparency, whilst the deep lying VBM enables efficient hole-blocking. The combination of TCTA and ZnO should enable efficient confinement of injected holes and electrons within the emitting perovskite layer, thus allowing for efficient radiative recombination. The use of ITO/ZnO/PEI and MoO_x/Ag electrodes ensures lossless injection of electrons and holes, respectively, in order to enable ohmic carrier injection. Thus, the selected *p*-*i*-*n* device structure should ensure efficient charge injection into and strong confinement of charge carriers within the perovskite emitting layer, which should be beneficial for high EL performance.

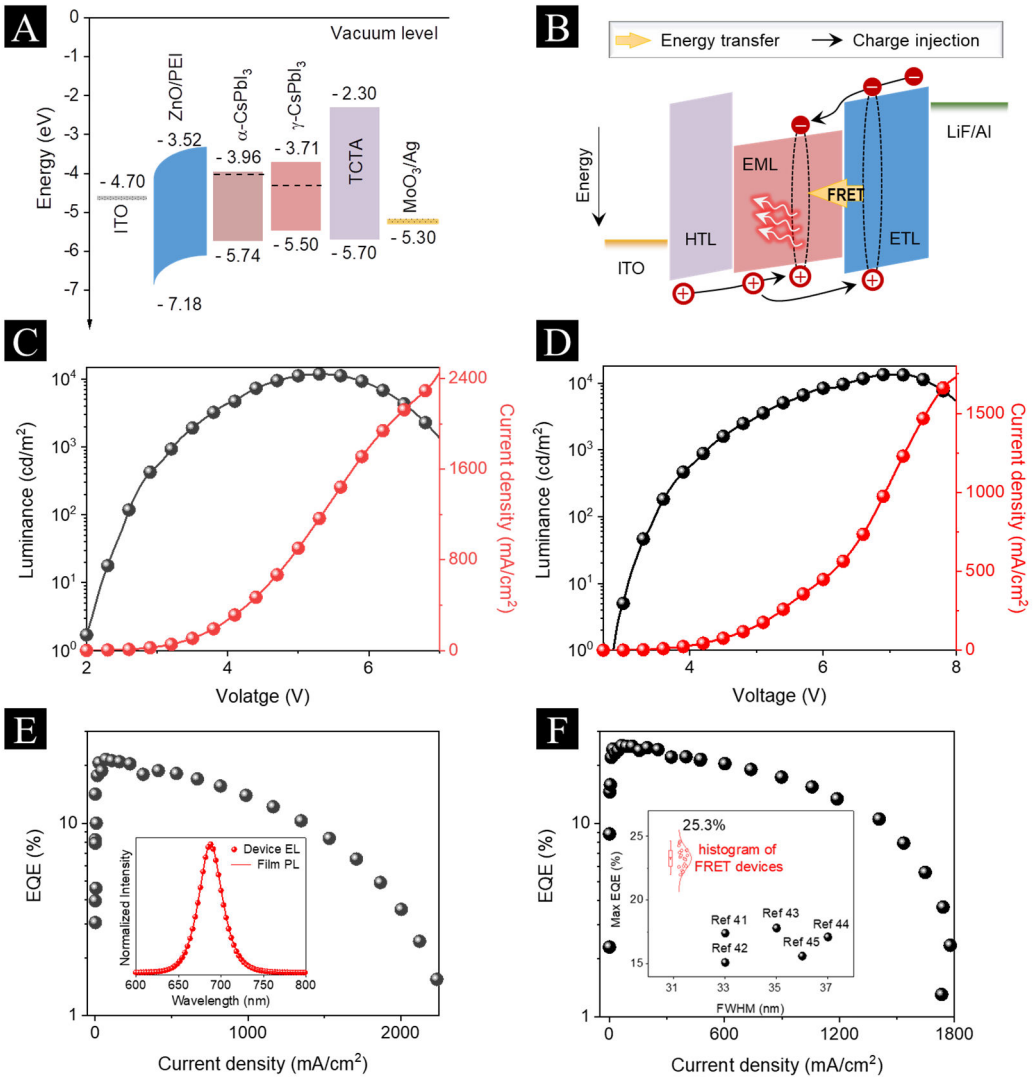

Figure. 5. Impact of the emitter structure on LED performance. (**A**) Energy level diagram for all layers of the *p-i-n* structured LEDs based on α-$CsPbI_3$ and γ-$CsPbI_3$ NCs. (**B**) Schematic diagram of the emitter excitation via direct charge injection and energy transfer which occurs in the FRET-LEDs. (**C**) and (**D**) Current density (red curve) and luminance (black curve) versus driving voltage of the LEDs of *p-i-n* structured and FRET LED. (**E**) External quantum efficiency versus current density of the *p-i-n* structured LEDs; inset compares normalized PL spectrum of the film and EL spectrum of LEDs based on γ-$CsPbI_3$ NCs. (**F**) External quantum efficiency versus current density of the FRET LED; the red curve in inset is a summary of the histogram of the FRET LED data; the black dots in the inset provide a summary of the reported EQE values for deep-red perovskite NCs LED with EQE > 15% from refs.[41-45]

Figure 5C shows the current density-voltage-luminance curves of the *p-i-n* structured LEDs based on γ-$CsPbI_3$ NCs. The *p-i-n* structured device has a low turn-on voltage of ~1.90 V and a high brightness of 11,862 cd m^{-2}, confirming that a highly efficient and barrier-free charge injection into the NCs was realized here. A high peak external quantum efficiency (EQE) of 21.5% was achieved for *p-i-n* structured LEDs (**Figure 5E**). In comparison, the α-$CsPbI_3$ NC based device has a higher turn-on voltage of ~2.05 V, a rather low EQE of 5.7%, and much lower peak brightness of 632 cd m^{-2} (**Figure S17**). The inset in **Figure 5E** compares normalized film PL and device EL spectra of γ-$CsPbI_3$ NCs, which are perfectly matching each other. Importantly, the EL signal originates solely from the γ-$CsPbI_3$ NCs without any noticeable contribution from any charge transport materials, indicating that the perovskite NC emitters serve as primary exciton recombination centers during device operation and further suggesting that balanced charge carrier transport was achieved.[46] In addition, the EL peak maintains the same spectral profile upon increasing the driving voltage (**Figure S18**), indicating that the emitting centers within the γ-$CsPbI_3$ NC film are stable under LED operation. Angle-dependent EL measurements (**Figure S19**) reveal that the radiation distribution is Lambertian. The EL stability of the two devices under continuous operation at a constant voltage of 3.5 V was evaluated. As shown in **Figure S20**, the EL signal of α-$CsPbI_3$ NC based LEDs drops down to 50% of its initial value after just 90 s, while the γ-$CsPbI_3$ NC based LEDs showed an operational stability for about 14 h.

As estimated from the current-voltage curves of the hole-only and electron-only

devices (**Figure S14**), γ-$CsPbI_3$ NCs have an electron mobility of 1.7×10^{-3} cm^2 $V^{-1}s^{-1}$ and a hole mobility of 3.3×10^{-3} cm^2 $V^{-1}s^{-1}$. For the *p-i-n* structured LEDs, the higher mobility of holes over electrons can be balanced through optimizing the thickness of the ZnO ETL and the TCTA HTL. However, as a result of the smooth charge carrier transport pathways and the high exciton binding energy of the quantum-confined nanometer-sized perovskite NCs, the easily injected charges tend to reach their saturation concentration within the perovskite emitting layer even at a low voltage, which results in charging of the γ-$CsPbI_3$ NCs and thus limits the LED performance. This phenomenon is evidenced by the current density-voltage-luminescence curves shown in **Figure 5C**, where the γ-$CsPbI_3$ NC based LED reaches the peak brightness at a low voltage of ~5 V, and it needs only ~ 3 V further increase to reach the maximum brightness after the device is turned on (deemed as when the brightness of a LED reaches 1 cd cm^{-2}). On the other hand, it is known that for NC-based LEDs, the emitters can be excited either by directly injected holes and electrons (like in the mentioned *p-i-n* structure), or by accepting an exciton from a nearby donor *via* Förster Resonance Energy Transfer (FRET). If both of the excitation mechanisms take place simultaneously, some of the injected charges would form excitons within the donor species and thus prevent the NCs from becoming charged. FRET occurs when there is sufficient spectral overlap between the PL of the donor and the NC absorption, and it has been previously proved that the FRET process between tris-(1-phenyl-1*H*-benzimidazole) (TPBi) molecules and red emitting semiconductor NCs (such as CdSe and ZnCuInS) can be highly efficient.[47, 48] Thus, it should be possible to realize both of

the mentioned NC excitation routes in our γ-$CsPbI_3$ NC based LEDs by making use of the TPBi layer, which was also confirmed by a set of PL spectra shown in **Figure S21**. One can see that the PL spectrum of γ-a mixture of $CsPbI_3$ NCs and TPBi in solution exhibits both peaks from γ-$CsPbI_3$ NCs and TPBi, indicating that the energy transfer between them is inefficient. Transformation of this solution into film obviously reduces the distance between γ-$CsPbI_3$ NCs and TPBi molecules, which promotes the FRET efficiency as evidenced by the disappeared PL emission of TPBi and enhanced PL intensity of the γ-$CsPbI_3$ NCs.

The respective LEDs made to verify this assumption (we call them FRET-LEDs further on) had a structure of ITO/PEDOT:PSS/poly-TPD/ γ-$CsPbI_3$ NCs/TPBi/LiF/Al, where PEDOT:PSS is poly(3,4-ethylenedioxythiophene) polystyrene sulfonate and poly-TPD is poly(N,N'-bis(4-butylphenyl)-N,N'-bis(phenyl)-benzidine). In this structure, the highly conductive PEDOT:PSS film helps to realize ohmic contact allowing lossless hole injection, while poly-TPD and TPBi are employed as hole-transport and electron-transport materials, respectively. The hole mobility of poly-TPD is 1.0×10^{-4} cm^2 $V^{-1}s^{-1}$,[49] which is an order of magnitude higher than the electron mobility of TPBi (~3.0×10^{-5} cm^2 $V^{-1}s^{-1}$).[50] As illustrated in **Figure 5B**, holes can transport towards the TPBi layer where they interact with electrons forming excitons, which then transfer towards the emitting layer of γ-$CsPbI_3$ NCs via the FRET process.

Figure 5D shows the current density-voltage-luminance curves of the γ-$CsPbI_3$ NC based LEDs designed to operate via the FRET excitation route. Their turn-on voltage slightly increases to ~2.9 V as compared with ~1.9 V of the previously

described *p-i-n* structured devices, which indicates a somewhat less efficient charge injection. At the same time, as shown in **Figure 5D and 5F**, the maximum brightness and peak EQE the FRET-LEDs increase to 13,626 cd m^{-2} and 25.3%, respectively. The voltage corresponding to the peak brightness increases to ~7 V, and the voltage difference extends to ~4 V between 1 cd cm^{-2} and the maximum brightness, which is ~1 V greater when compared to that of the *p-i-n* structured devices. To the best of our knowledge, the brightness of our devices is the highest value among all reported perovskite and organic LEDs (**Table S5**), and the achieved peak EQE (25.3%) of the FRET-LEDs is the highest value among any reported red-emitting perovskite NC LEDs (see the inset of **Figure 5F and Table S6**). Compared with the *p-i-n* structure of LEDs, we estimate contribution of the FRET process to overall EQE as ~10%, as discussed in Supporting Information in relation to data presented in **Figure S22**. **Figure S23** shows the EQE histogram of 20 FRET-LEDs test devices, from which the high average EQE of 23.5% has been derived. The current efficiency and power efficiency are 2.1 cd/A and 1.7%, as shown in **Figure S24**.

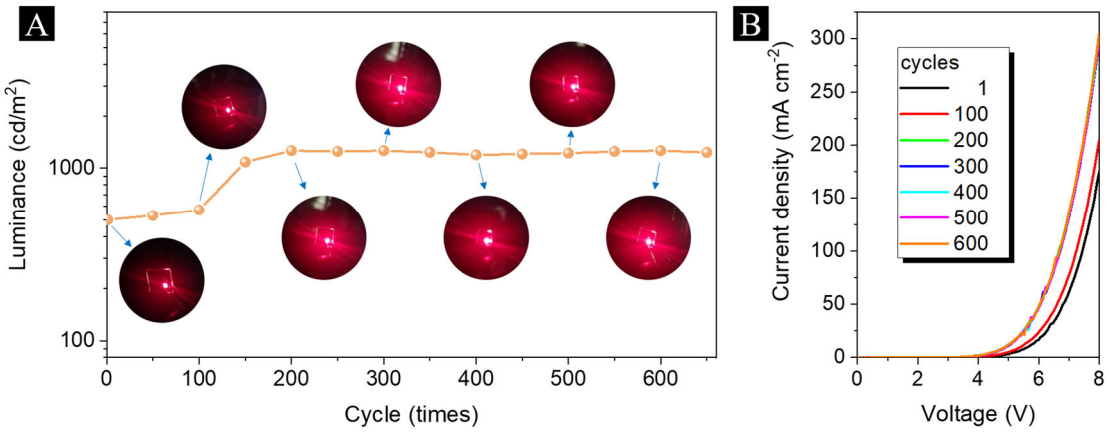

Figure. 6. Repeatedly illumination test of FRET-LEDs. The FRET-LED was illuminated repeatedly at an initial brightness of 500 cd m^{-2} at a constant voltage range.

(**A**) Photographs illustrating brightness of the FRET-LED illuminated up to 600 times, and a respective change of luminance of these devices versus number of repeated cycles. (**B**) Current density versus driving voltage curves of the FRET-LED at different illumination cycles.

Another advantage of the FRET-LEDs is that the electric field applied to the *γ*-$CsPbI_3$ NCs is reduced, which should result in the improved device stability. Indeed, for the *p-i-n* structured LEDs, the device stops emitting light when the applied voltage reaches 7 V, whilst FRET-LEDs continue to operate even at voltage of 9 V. As illustrated by the photograph provided in **Figure S25**, FRET-LEDs can be lit repeatedly for three times at least, maintaining their bright and stable red emission. Surface temperature monitoring of the FRET-LED during operation under a constant voltage of 7 V over a duration of 12 min for three consecutive times shows negligible generation of Joule heat (**Figure S25**), and the device temperature remains unchanged at ~25 °C, demonstrating that high carrier concentration induced NC charging is indeed suppressed within the FRET-LEDs. Since LED operation requires applications have repeated on-and-off scenarios, we examined the changes in brightness and current by performing repeated on/off tests on a FRET-LED at initial brightness of 500 cd m^{-2} and a constant voltage range (**Figure 6**). After 200 repetitions, the device brightness reaches ~1200 cd m^{-2} (**Figure 6A**), and the FRET-LED in equilibrium shows excellent stability, with no change in current densities (**Figure 6B**) or brightness after 650 repetitions. Such device stability meets the requirements of practical LED applications and indicates the excellent commercial potential of FRET-LEDs based on the *γ*-$CsPbI_3$ NCs.

Conclusions

In conclusion, we developed a seed-assisted growth strategy to induce formation of γ-$CsPbI_3$ NCs using ultrasmall CaI_x nanoparticles as the seeds. This allowed us not only to control the crystal phase of the perovskite NCs, but also to decorate their surface with additionally adsorbed CaI_2 NCs providing passivating outer shells. The bright and stable seed/core/shell CaI_x/γ-$CsPbI_3$/CaI_2 NCs possess a type-I energy structure which is beneficial for confining charge carriers and thus enables efficient radiative recombination. As a result, compared with α-$CsPbI_3$ NCs, γ-$CsPbI_3$ NCs show significantly improved optical and electrical properties and ~25 times higher structural stability. Two different sets of LEDs based on γ-$CsPbI_3$ NC films as the light-emitting layers were fabricated to elucidate the different EL mechanisms, and it was revealed that the emitters excited by direct charge injection and FRET simultaneously offer high efficiency along with excellent stability. The FRET-LEDs achieved a record EQE of 25.3% (average value 23.5% among 20 devices tested) and a high brightness of 13,626 cd/m^2, which to the best of our knowledge is the highest value among any reported red-emitting perovskite NC LEDs. These devices can repeatedly be illuminated over 650 times at ~500 cd/m^2 with no decline of brightness, which indicates their great commercial potential. The results of our study suggest that orthorhombic γ-$CsPbI_3$ perovskite NCs are excellent candidates for optoelectronic applications.

Materials and Methods

Materials: Oleic acid (OA, 90%), 1-octadecene (ODE, 90%), MoO_3 and PbI_2 (99.999%) were purchased from Alfa Aesar. Oleylamine (OLA, 80-90%) was

purchased from Aladdin. CaI_2 (99%), zinc acetate, sodium hydroxide, and LiF were purchased from Sigma-Aldrich. Cs_2CO_3 (99.9%) was purchased from J&K. 4,4′-bis(carbazole-9-yl)biphenyl and 4,4′,4″-tris(carbazol-9-yl)triphenylamine (TCTA), poly(3,4-ethylenedioxythiophene): poly(styrenesulfonate) (PEDOT:PSS) (4083), poly(N,N'-bis(4-butylphenyl)-N,N'-bis(phenyl)-benzidine) (poly-TPD) and tris-(1-phenyl-1*H*-benzimidazole) (TPBi) were purchased from XiAn Polymer Light Technology Corp. All chemicals were used directly without further purification.

Synthesis of perovskite NCs: All the operations were conducted at room temperature, with an indoor humidity of 60-80%. Cesium oleate was prepared by adding Cs_2CO_3 (814.0 mg), OA (2.5 mL), and ODE (30.0 mL) into a 100 mL three-neck flask; the mixture was degassed and dried under vacuum for 1 h at 120 ˚C, and heated to 150 ˚C under N_2 until a clear solution was obtained.

For the synthesis of α-phase $CsPb_yCa_{1-y}I_3$ ($0<y\leqslant 1$) NCs and γ-$CsPbI_3$ NCs, the only variable was the feeding ratio of the CaI_2 and PbI_2 precursors ($R_{<Ca/Pb>}$), namely the dosage of PbI_2 remained the same (0.376 mmol, 173.0 mg) while the CaI_2 amount was adjusted accordingly. For example, when $R_{<Ca/Pb>}$ equaled 0.5, we loaded 10.0 mL ODE, 0.376 mmol PbI_2 (173.0 mg), and 0.188 mmol CaI_2 (55.3 mg) into a 50 mL three-neck flask, then degassed and dried by applying vacuum for 1 h at 120 ˚C. 1.0 mL OLA and 1.0 mL OA were quickly injected, the temperature was raised to 170 ˚C, and 1.0 mL of cesium oleate solution was quickly injected. After 5 s, the reaction mixture was cooled down to room temperature in an ice-water bath. The reaction product was separated by centrifugation for 10 min at 5000 rpm; the precipitate was redispersed in

2.0 mL of toluene, 2.0 mL ethyl acetate was added, the mixture was centrifuged for 10 min at 10000 rpm, and the precipitate was redispersed in 1.0 mL of toluene.

Synthesis of ZnO NCs: A mixture of 0.4403 g of zinc acetate and 30.0 mL of ethyl alcohol were loaded into a 250 mL three-neck flask. After 10 min nitrogen flow, the flask was heated with stirring until the zinc acetate was completely dissolved whereupon the solution became colorless and transparent. The flask was cooled to room temperature naturally and the solution became white and turbid. Then, a mixture of 0.2 g of sodium hydroxide and 10 mL of ethyl alcohol were swiftly injected into the flask and stirring was maintained for 4 h. Finally, 5 mL of the as obtained ZnO NC solution was loaded into a 50 mL centrifuge tube, and hexane was added to fill up the tube. After centrifugation of this solution, the precipitate was dissolved in 3 mL of ethyl alcohol. The purification was executed one more time.

Device fabrication: Patterned ITO-coated glasses were cleaned successively using soap, deionized water, ethanol, chloroform, acetone, and isopropanol, and subjected to UV-ozone treatment for 15 min. For the *p-i-n* structured LEDs, a solution of ZnO NCs was spin-coated onto the ITO substrate at 1000 rpm for 40 seconds and annealed in air at 150 ˚C for 10 min. The substrate was transferred into an N_2 glove-box, a PEI 2-methoxyethanol solution (0.2% mass fraction) was spin-coated onto the ZnO film at a speed of 4000 rpm and annealed at 150 ˚C for 10 min. The γ-$CsPbI_3$ NCs were spin-cast at 1000 rpm for 40 s. TCTA, MoO_x, and Ag layers were sequentially deposited by thermal evaporation in a vacuum deposition chamber (~1×10^{-4} Pa pressure).

For the FRET-LEDs, the PEDOT:PSS solution was spin-coated onto the ITO-coated glass substrate at 4000 rpm for 40 s and annealed in air at 150 °C for 15 min. The substrate was transferred into a N_2 filled glove-box; poly-TPD chlorobenzene solution (concentration of 8 mg mL^{-1}) was spin-coated on top of the PEDOT:PSS at 4000 rpm for 40 s and annealed at 150 ˚C for 15 min; this layer was regarded as the hole transport layer and electron blocking layer. The γ-$CsPbI_3$ NCs were deposited by spin-coating at 1000 rpm for 40 s. TPBi (40 nm thickness) electron transport layer and LiF/Al electrodes (1 nm/100 nm respectively) were sequentially deposited by thermal evaporation in a vacuum deposition chamber (~1×10^{-4} Pa pressure).

Characterization: Absorption and photoluminescence (PL) spectra were measured on a Perkin Elmer Lambda 950 spectrometer and a Cary Eclipse spectrofluorimeter, respectively. Transmission electron microscopy (TEM) images were obtained on a FEI Tecnai F20 microscope. Scanning electron microscopy (SEM) images were obtained on a JEOL JSM-7500F system. XRD data were collected on a Bruker SMART-CCD diffractometer. The absolute PL QYs of the samples were measured with a fluorescence spectrometer (FLS920P, Edinburgh Instruments) equipped with an integrating sphere with its inner face coated with BENFLEC. X-ray photoelectron spectroscopy (XPS) was performed on an ESCALAB250 spectrometer. Time-resolved PL measurements were conducted on a time correlated single-photon counting system of the FLS920P spectrometer. A 375 nm picosecond diode laser (EPL-375, repetition rate up to 20 MHz, pulse width 64.8 ps) was used to excite the samples. Ultraviolet photoelectron spectra (UPS) were collected using a PREVAC system. The J-V-L characteristics and the EL spectra of the LEDs were collected using a Keithley 2400 source meter and a Photo Research spectrometer PR650 with samples under an adhesive encapsulation and in a

dark room. Regarding the LED performance, we calibrated the data using a commercially available system (from SHENZHEN PYNECT SCIENCE AND TECHNOLOGY CO., LTD.), where a Keithley 2400 source meter was utilized to obtain current density–voltage characteristics, and a fiber integration sphere coupled with a QE Pro spectrometer was used for light output measurements. Such kind of system is widely used in testing OLEDs and QLEDs.[54]

First-principles density functional theory (DFT): Calculations were performed using the projected augmented wave (PAW).[55] The Perdew-Burke-Ernzerhof exchange-correlation functional of the generalized-gradient approximation (PBE-GGA) with vdW[56] corrections was adopted for the exchange-correlation functional. In all calculations, the plane-wave expansion of the wave functions with an energy cutoff of 400 eV was applied. During the relaxation, the force tolerance was set to 0.05 eV/Å. The binding energy was calculated as E - E_a - E_b, where E is the total energy of the adsorbed system, and E_a and E_b represent the total energy of free species respectively. All calculations were performed by Vienna ab initio Simulation Package (VASP).

Author information

Corresponding Authors

Xiaoyu Zhang - Key Laboratory of Automobile Materials MOE, School of Materials Science & Engineering, and Jilin Provincial International Cooperation Key Laboratory of High-Efficiency Clean Energy Materials, Jilin University, Changchun 130012, China; E-mail: zhangxiaoyu@jlu.edu.cn (X.Z.);

Yu Zhang - State Key Laboratory of Integrated Optoelectronics, College of Electronic Science and Engineering, Jilin University, Changchun 130012, P.R. China; E-mail:

yuzhang@jlu.edu.cn (Y.Z.);

Weitao Zheng - Key Laboratory of Automobile Materials MOE, School of Materials Science & Engineering, and Jilin Provincial International Cooperation Key Laboratory of High-Efficiency Clean Energy Materials, Jilin University, Changchun 130012, China; E-mail: wtzheng@jlu.edu.cn (W.Z.);

Andrey L. Rogach - Department of Materials Science and Engineering, and Centre for Functional Photonics (CFP), City University of Hong Kong, Hong Kong S.A.R 999077, P.R. China; E-mail:andrey.rogach@cityu.edu.hk

Authors

Jie Guo - Key Laboratory of Automobile Materials MOE, School of Materials Science & Engineering, and Jilin Provincial International Cooperation Key Laboratory of High-Efficiency Clean Energy Materials, Jilin University, Changchun 130012, China

Min Lu - State Key Laboratory of Integrated Optoelectronics, College of Electronic Science and Engineering, Jilin University, Changchun 130012, P.R. China

Siqi Sun - State Key Laboratory of Integrated Optoelectronics, College of Electronic Science and Engineering, Jilin University, Changchun 130012, P.R. China

Ce Han - Key Laboratory of Automobile Materials MOE, School of Materials Science & Engineering, and Jilin Provincial International Cooperation Key Laboratory of High-Efficiency Clean Energy Materials, Jilin University, Changchun 130012, China

Xuyong Yang - Key Laboratory of Advanced Display and System Applications of Ministry of Education, Shanghai University, Shanghai 200072, P.R. China

Stephen V. Kershaw - Department of Materials Science and Engineering, and Centre for Functional Photonics (CFP), City University of Hong Kong, Hong Kong S.A.R 999077, P.R. China

Author Contributions

X.Z., Y.Z., W.Z. and A.L.R designed and directed the study. J.G. and M.L. fabricated and characterized LEDs. J.G. synthesized the perovskite NCs. S.V.K. analyzed the TA data. J.G., M.L., X.Z., S.S., Y.Z., X.Y., S.V.K., W.Z., and A.L.R. analyzed and discussed the experimental results. All authors contributed to writing the manuscript. J.G. and M.L. contributed equally to this work.

Competing financial interests

The authors declare no competing financial interest.

Data availability

The data that support the findings of this study are available from the corresponding author upon reasonable request.

Acknowledgements

National Key Research and Development Program of China (project 2022YFE0200200)

National Natural Science Foundation of China (52072141, 51972136)

Interdisciplinary Integration and Innovation Project of JLU (JLUXKJC2021QZ12)

Research Grant Council of Hong Kong (C7035-20G)

Project MHP/068/21 from the Innovation and Technology Commission of Hong Kong

References

(1) Lu, M.; Guo, J.; Sun, S.; Lu, P.; Zhang, X.; Shi, Z.; Yu, W. W.Zhang, Y. Surface ligand engineering-assisted $CsPbI_3$ quantum dots enable bright and efficient red light-emitting diodes with a top-emitting structure. *Chem. Eng. J.* **2021,** *404*, 126563.

(2) Protesescu, L.; Yakunin, S.; Bodnarchuk, M. I.; Krieg, F.; Caputo, R.; Hendon, C. H.; Yang, R. X.; Walsh, A.Kovalenko, M. V. Nanocrystals of Cesium Lead Halide

Perovskites ($CsPbX_3$, X = Cl, Br, and I): Novel Optoelectronic Materials Showing Bright Emission with Wide Color Gamut. *Nano Lett.* **2015,** *15* (6), 3692-3696.

(3) Steele, J. A.; Jin, H.; Dovgaliuk, I.; Berger, R. F.; Braeckevelt, T.; Yuan, H.; Martin, C.; Solano, E.; Lejaeghere, K.; Rogge, S. M. J.; Notebaert, C.; Vandezande, W.; Janssen, K. P. F.; Goderis, B.; Debroye, E.; Wang, Y.-K.; Dong, Y.; Ma, D.; Saidaminov, M.; Tan, H.; Lu, Z.; Dyadkin, V.; Chernyshov, D.; Van Speybroeck, V.; Sargent, E. H.; Hofkens, J.Roeffaers, M. B. J. Thermal unequilibrium of strained black $CsPbI_3$ thin films. *Sci.* **2019,** *365* (6454), 679-684.

(4) Zhang, X.; Zeng, Q.; Xiong, Y.; Ji, T.; Wang, C.; Shen, X.; Lu, M.; Wang, H.; Wen, S.; Zhang, Y.; Yang, X.; Ge, X.; Zhang, W.; Litvin, A. P.; Baranov, A. V.; Yao, D.; Zhang, H.; Yang, B.; Rogach, A. L.Zheng, W. Energy Level Modification with Carbon Dot Interlayers Enables Efficient Perovskite Solar Cells and Quantum Dot Based Light-Emitting Diodes. *Adv. Funct. Mater.* **2020,** *30* (11), 1910530.

(5) Qiu, F.-Z.; Li, M.-H.; Qi, J.-J.; Jiang, Y.Hu, J.-S. Engineering inorganic lead halide perovskite deposition toward solar cells with efficiency approaching 20%. *Aggregate* **2021,** *2* (1), 66-83.

(6) Wu, J.; Liu, S.-C.; Li, Z.; Wang, S.; Xue, D.-J.; Lin, Y.Hu, J.-S. Strain in perovskite solar cells: origins, impacts and regulation. *Natl. Sci. Rev.* **2021,** *8* (8), nwab047.

(7) Liu, S.-C.; Li, Z.; Yang, Y.; Wang, X.; Chen, Y.-X.; Xue, D.-J.Hu, J.-S. Investigation of Oxygen Passivation for High-Performance All-Inorganic Perovskite Solar Cells. *J. Am. Chem. Soc.* **2019,** *141* (45), 18075-18082.

(8) Gkotsi, D.; Begum, R.; Salt, T.; Lascaratos, G.; Hogg, C.; Chau, K.-Y.; Schapira, A. H. V.Jeffery, G. Recharging mitochondrial batteries in old eyes. Near infra-red increases ATP. *Exp. Eye Res.* **2014,** *122*, 50-53.

(9) Sivapathasuntharam, C.; Sivaprasad, S.; Hogg, C.Jeffery, G. Improving mitochondrial function significantly reduces the rate of age related photoreceptor loss. *Exp. Eye Res.* **2019,** *185*, 107691.

(10)Hong, G.; Antaris, A. L.Dai, H. Near-infrared fluorophores for biomedical imaging. *Nat. Biomed. Eng.* **2017,** *1* (1), 0010.

(11) Ren, A.; Wang, H.; Zhang, W.; Wu, J.; Wang, Z.; Penty, R. V.White, I. H. Emerging

light-emitting diodes for next-generation data communications. *Nat. Electron.* **2021,** *4* (8), 559-572.

(12) Swarnkar, A.; Mir, W. J.Nag, A. Can B-Site Doping or Alloying Improve Thermal- and Phase-Stability of All-Inorganic $CsPbX_3$ (X = Cl, Br, I) Perovskites? *ACS Energy Lett.* **2018,** *3* (2), 286-289.

(13) Sutton, R. J.; Filip, M. R.; Haghighirad, A. A.; Sakai, N.; Wenger, B.; Giustino, F.Snaith, H. J. Cubic or Orthorhombic? Revealing the Crystal Structure of Metastable Black-Phase $CsPbI_3$ by Theory and Experiment. *ACS Energy Lett.* **2018,** *3* (8), 1787-1794.

(14) Wang, K.; Jin, Z.; Liang, L.; Bian, H.; Wang, H.; Feng, J.; Wang, Q.Liu, S. Chlorine doping for black γ-$CsPbI_3$ solar cells with stabilized efficiency beyond 16%. *Nano Energy* **2019,** *58*, 175-182.

(15) Zhao, B.; Jin, S.-F.; Huang, S.; Liu, N.; Ma, J.-Y.; Xue, D.-J.; Han, Q.; Ding, J.; Ge, Q.-Q.Feng, Y. Thermodynamically stable orthorhombic γ-$CsPbI_3$ thin films for high-performance photovoltaics. *J. Am. Chem. Soc.* **2018,** *140* (37), 11716-11725.

(16) Sun, J.-K.; Huang, S.; Liu, X.-Z.; Xu, Q.; Zhang, Q.-H.; Jiang, W.-J.; Xue, D.-J.; Xu, J.-C.; Ma, J.-Y.; Ding, J.; Ge, Q.-Q.; Gu, L.; Fang, X.-H.; Zhong, H.-Z.; Hu, J.-S.Wan, L.-J. Polar Solvent Induced Lattice Distortion of Cubic $CsPbI_3$ Nanocubes and Hierarchical Self-Assembly into Orthorhombic Single-Crystalline Nanowires. *J. Am. Chem. Soc.* **2018,** *140* (37), 11705-11715.

(17) Steele Julian, A.; Jin, H.; Dovgaliuk, I.; Berger Robert, F.; Braeckevelt, T.; Yuan, H.; Martin, C.; Solano, E.; Lejaeghere, K.; Rogge Sven, M. J.; Notebaert, C.; Vandezande, W.; Janssen Kris, P. F.; Goderis, B.; Debroye, E.; Wang, Y.-K.; Dong, Y.; Ma, D.; Saidaminov, M.; Tan, H.; Lu, Z.; Dyadkin, V.; Chernyshov, D.; Van Speybroeck, V.; Sargent Edward, H.; Hofkens, J.Roeffaers Maarten, B. J. Thermal unequilibrium of strained black $CsPbI_3$ thin films. *Science* **2019,** *365* (6454), 679-684.

(18) Wang, Y.-K.; Yuan, F.; Dong, Y.; Li, J.-Y.; Johnston, A.; Chen, B.; Saidaminov, M. I.; Zhou, C.; Zheng, X.; Hou, Y.; Bertens, K.; Ebe, H.; Ma, D.; Deng, Z.; Yuan, S.; Chen, R.; Sagar, L. K.; Liu, J.; Fan, J.; Li, P.; Li, X.; Gao, Y.; Fung, M.-K.; Lu, Z.-H.; Bakr, O. M.; Liao, L.-S.Sargent, E. H. All-Inorganic Quantum-Dot LEDs Based on a Phase-

Stabilized α-$CsPbI_3$ Perovskite. *Angew. Chem. Int. Ed.* **2021,** *60* (29), 16164-16170.

(19) Lan, Y.-F.; Yao, J.-S.; Yang, J.-N.; Song, Y.-H.; Ru, X.-C.; Zhang, Q.; Feng, L.-Z.; Chen, T.; Song, K.-H.Yao, H.-B. Spectrally Stable and Efficient Pure Red $CsPbI_3$ Quantum Dot Light-Emitting Diodes Enabled by Sequential Ligand Post-Treatment Strategy. *Nano Lett.* **2021,** *21* (20), 8756-8763.

(20) Wang, Y.-K.; Singh, K.; Li, J.-Y.; Dong, Y.; Wang, X.-Q.; Pina, J. M.; Yu, Y.-J.; Sabatini, R.; Liu, Y.; Ma, D.; Liu, J.; Liu, Z.; Gao, Y.; Voznyy, O.; Ma, W.; Fung, M.-K.; Liao, L.-S.Sargent, E. H. In-situ inorganic ligand replenishment enables bandgap stability in mixed-halide perovskite quantum dot solids. *Adv. Mater.* **2022,** *34* (21), 2200854.

(21) Guo, J.; Fu, Y.; Lu, M.; Zhang, X.; Kershaw, S. V.; Zhang, J.; Luo, S.; Li, Y.; Yu, W. W.; Rogach, A. L.; Zhang, L.Bai, X. Cd-Rich Alloyed $CsPb_{1-x}CdxBr_3$ Perovskite Nanorods with Tunable Blue Emission and Fermi Levels Fabricated through Crystal Phase Engineering. *Adv. Sci.* **2020,** *7* (15), 2000930.

(22) Lu, M.; Zhang, X.; Zhang, Y.; Guo, J.; Shen, X.; Yu, W. W.Rogach, A. L. Simultaneous Strontium Doping and Chlorine Surface Passivation Improve Luminescence Intensity and Stability of $CsPbI_3$ Nanocrystals Enabling Efficient Light-Emitting Devices. *Adv. Mater.* **2018,** *30* (50), 1804691.

(23) Shen, W.; Zhang, J.; Dong, R.; Chen, Y.; Yang, L.; Chen, S.; Su, Z.; Dai, Y.; Cao, K.Liu, L. Stable and Efficient Red Perovskite Light-Emitting Diodes Based on Ca^{2+}-Doped $CsPbI_3$ Nanocrystals. *Research* **2021,** *2021*, DOI:10.34133/2021/9829374.

(24) Wang, S.; Bi, C.; Portniagin, A.; Yuan, J.; Ning, J.; Xiao, X.; Zhang, X.; Li, Y. Y.; Kershaw, S. V.; Tian, J.Rogach, A. L. $CsPbI_3$/PbSe Heterostructured Nanocrystals for High-Efficiency Solar Cells. *ACS Energy Lett.* **2020,** *5* (7), 2401-2410.

(25) Zhang, X.; Yin, W.; Zheng, W.Rogach, A. L. Perovskite Quantum Dots with Atomic Crystal Shells for Light-Emitting Diodes with Low Efficiency Roll-Off. *ACS Energy Lett.* **2020,** *5* (9), 2927-2934.

(26) Yi, C.; Liu, C.; Wen, K.; Liu, X.-K.; Zhang, H.; Yu, Y.; Fan, N.; Ji, F.; Kuang, C.; Ma, B.; Tu, C.; Zhang, Y.; Xue, C.; Li, R.; Gao, F.; Huang, W.Wang, J. Intermediate-phase-assisted low-temperature formation of γ-$CsPbI_3$ films for high-efficiency deep-

red light-emitting devices. *Nat. Commun.* **2020,** *11*, 4736.
(27) Wang, B.; Novendra, N.Navrotsky, A. Energetics, Structures, and Phase Transitions of Cubic and Orthorhombic Cesium Lead Iodide ($CsPbI_3$) Polymorphs. *J. Am. Chem. Soc.* **2019,** *141* (37), 14501-14504.
(28) Zhao, H.; Xu, J.; Zhou, S.; Li, Z.; Zhang, B.; Xia, X.; Liu, X.; Dai, S.Yao, J. Preparation of Tortuous 3D γ-$CsPbI_3$ Films at Low Temperature by CaI_2 as Dopant for Highly Efficient Perovskite Solar Cells. *Adv. Funct. Mater.* **2019,** *29* (27), 1808986.
(29) Liu, F.; Zhang, Y.; Ding, C.; Kobayashi, S.; Izuishi, T.; Nakazawa, N.; Toyoda, T.; Ohta, T.; Hayase, S.; Minemoto, T.; Yoshino, K.; Dai, S.Shen, Q. Highly Luminescent Phase-Stable $CsPbI_3$ Perovskite Quantum Dots Achieving Near 100% Absolute Photoluminescence Quantum Yield. *ACS Nano* **2017,** *11* (10), 10373-10383.
(30) Zhang, X.; Lu, M.; Zhang, Y.; Wu, H.; Shen, X.; Zhang, W.; Zheng, W.; Colvin, V. L.Yu, W. W. PbS Capped $CsPbI_3$ Nanocrystals for Efficient and Stable Light-Emitting Devices Using p–i–n Structures. *ACS Cent. Sci.* **2018,** *4* (10), 1352-1359.
(31) Bai, Y.; Hao, M.; Ding, S.; Chen, P.Wang, L. Surface Chemistry Engineering of Perovskite Quantum Dots: Strategies, Applications, and Perspectives. *Adv. Mater.* **2022,** *34* (4), 2105958.
(32) Gao, Q.; Qi, J.; Chen, K.; Xia, M.; Hu, Y.; Mei, A.Han, H. Halide Perovskite Crystallization Processes and Methods in Nanocrystals, Single Crystals and Thin Films. *Adv. Mater.* **2022,** *2022,* DOI: 10.1002/adma.202200720.
(33) Cho, N.-K.; Na, H.-J.; Yoo, J.Kim, Y. S. Long-term stability in γ-$CsPbI_3$ perovskite via an ultraviolet-curable polymer network. *Commun. Mater.* **2021,** *2* (1), 30.
(34) Khan, A. A.; Azam, M.; Eric, D.; Liang, G.Yu, Z. Triple cation perovskite doped with the small molecule F4TCNQ for highly efficient stable photodetectors. *J. Mater. Chem. C* **2020,** *8* (8), 2880-2887.
(35) Bi, D.; Yi, C.; Luo, J.; Décoppet, J.-D.; Zhang, F.; Zakeeruddin, Shaik M.; Li, X.; Hagfeldt, A.Grätzel, M. Polymer-templated nucleation and crystal growth of perovskite films for solar cells with efficiency greater than 21%. *Nat. Energy* **2016,** *1* (10), 16142.
(36) Navas, J.; Sánchez-Coronilla, A.; Gallardo, J. J.; Cruz Hernández, N.; Piñero, J. C.; Alcántara, R.; Fernández-Lorenzo, C.; De los Santos, D. M.; Aguilar, T.Martín-Calleja,

J. New insights into organic–inorganic hybrid perovskite CH3NH3PbI3 nanoparticles. An experimental and theoretical study of doping in Pb^{2+} sites with Sn^{2+}, Sr^{2+}, Cd^{2+} and Ca^{2+}. *Nanoscale* **2015,** *7* (14), 6216-6229.

(37) Li, Y.; Huang, H.; Xiong, Y.; Richter, A. F.; Kershaw, S. V.; Feldmann, J.Rogach, A. L. Using Polar Alcohols for the Direct Synthesis of Cesium Lead Halide Perovskite Nanorods with Anisotropic Emission. *ACS Nano* **2019,** *13* (7), 8237-8245.

(38) Yin, W.; Li, M.; Dong, W.; Luo, Z.; Li, Y.; Qian, J.; Zhang, J.; Zhang, W.; Zhang, Y.; Kershaw, S. V.; Zhang, X.; Zheng, W.Rogach, A. L. Multidentate Ligand Polyethylenimine Enables Bright Color-Saturated Blue Light-Emitting Diodes Based on $CsPbBr_3$ Nanoplatelets. *ACS Energy Lett.* **2021,** *6* (2), 477-484.

(39) Dong, W.; Zhang, X.; Yang, F.; Zeng, Q.; Yin, W.; Zhang, W.; Wang, H.; Yang, X.; Kershaw, S. V.; Yang, B.; Rogach, A. L.Zheng, W. Amine-Terminated Carbon Dots Linking Hole Transport Layer and Vertically Oriented Quasi-2D Perovskites through Hydrogen Bonds Enable Efficient LEDs. *ACS Nano* **2022,** *16* (6), 9679-9690.

(40) Sun, S.; Jia, P.; Lu, M.; Lu, P.; Gao, Y.; Zhong, Y.; Tang, C.; Zhang, Y.; Wu, Z.; Zhu, J.; Zhang, Y.; Yu, W. W.Bai, X. Enhanced Flexibility and Stability of Emissive Layer Enable High-Performance Flexible Light-Emitting Diodes by Cross-Linking of Biomass Material. *Adv. Funct. Mater.* **2022,** *32* (33), 2204286.

(41) Lu, P.; Wu, J.; Shen, X.; Gao, X.; Shi, Z.; Lu, M.; Yu, W. W.Zhang, Y. ZnO–Ti_3C_2 MXene Electron Transport Layer for High External Quantum Efficiency Perovskite Nanocrystal Light-Emitting Diodes. *Adv. Sci.* **2020,** *7* (19), 2001562.

(42) Shen, X.; Zhang, Y.; Kershaw, S. V.; Li, T.; Wang, C.; Zhang, X.; Wang, W.; Li, D.; Wang, Y.; Lu, M.; Zhang, L.; Sun, C.; Zhao, D.; Qin, G.; Bai, X.; Yu, W. W.Rogach, A. L. Zn-Alloyed $CsPbI_3$ Nanocrystals for Highly Efficient Perovskite Light-Emitting Devices. *Nano Lett.* **2019,** *19* (3), 1552-1559.

(43) Li, H.; Lin, H.; Ouyang, D.; Yao, C.; Li, C.; Sun, J.; Song, Y.; Wang, Y.; Yan, Y.; Wang, Y.; Dong, Q.Choy, W. C. H. Efficient and Stable Red Perovskite Light-Emitting Diodes with Operational Stability >300 h. *Adv. Mater.* **2021,** *33* (15), 2008820.

(44) Chen, C.; Xuan, T.; Bai, W.; Zhou, T.; Huang, F.; Xie, A.; Wang, L.Xie, R.-J. Highly stable $CsPbI_3$:Sr^{2+} nanocrystals with near-unity quantum yield enabling perovskite

light-emitting diodes with an external quantum efficiency of 17.1%. *Nano Energy* **2021,** *85*, 106033.

(45) Yang, S.; Bi, C.; Dong, W.; Zhang, X.; Zheng, W.; Choy, W. C. H.Tian, J. Electron Delocalization in $CsPbI_3$ Quantum Dots Enables Efficient Light-Emitting Diodes with Improved Efficiency Roll-Off. *Adv. Opt. Mater.* **2022,** *10* (11), 2200189.

(46) Swarnkar, A.; Marshall, A. R.; Sanehira, E. M.; Chernomordik, B. D.; Moore, D. T.; Christians, J. A.; Chakrabarti, T.Luther, J. M. Quantum dot–induced phase stabilization of α-$CsPbI_3$ perovskite for high-efficiency photovoltaics. *Sci.* **2016,** *354* (6308), 92.

(47) Yuan, X.; Zhao, J.; Jing, P.; Zhang, W.; Li, H.; Zhang, L.; Zhong, X.Masumoto, Y. Size- and Composition-Dependent Energy Transfer from Charge Transporting Materials to ZnCuInS Quantum Dots. *J. Phys. Chem. C* **2012,** *116* (22), 11973-11979.

(48) Jing, P.; Yuan, X.; Ji, W.; Ikezawa, M.; Wang, Y. A.; Liu, X.; Zhang, L.; Zhao, J.Masumoto, Y. Shell-Dependent Energy Transfer from 1,3,5-Tris(N-phenylbenzimidazol-2,yl) Benzene to CdSe Core/Shell Quantum Dots. *J. Phys. Chem. C* **2010,** *114* (45), 19256-19262.

(49) Thesen, M. W.; Höfer, B.; Debeaux, M.; Janietz, S.; Wedel, A.; Köhler, A.; Johannes, H.-H.Krueger, H. Hole-transporting host-polymer series consisting of triphenylamine basic structures for phosphorescent polymer light-emitting diodes. *J. Polym. Sci., Part A: Polym. Chem.* **2010,** *48* (15), 3417-3430.

(50) Wu, I. W.; Wang, P.-S.; Tseng, W.-H.; Chang, J.-H.Wu, C.-I. Correlations of impedance–voltage characteristics and carrier mobility in organic light emitting diodes. *Org. Electron.* **2012,** *13* (1), 13-17.

(51) Bodnarchuk, M. I.; Boehme, S. C.; ten Brinck, S.; Bernasconi, C.; Shynkarenko, Y.; Krieg, F.; Widmer, R.; Aeschlimann, B.; Günther, D.; Kovalenko, M. V.Infante, I. Rationalizing and Controlling the Surface Structure and Electronic Passivation of Cesium Lead Halide Nanocrystals. *ACS Energy Lett.* **2019,** *4* (1), 63-74.

(52) Fiuza-Maneiro, N.; Sun, K.; López-Fernández, I.; Gómez-Graña, S.; Müller-Buschbaum, P.Polavarapu, L. Ligand Chemistry of Inorganic Lead Halide Perovskite Nanocrystals. *ACS Energy Lett.* **2023,** *8* (2), 1152-1191.

(53) De Roo, J.; Ibáñez, M.; Geiregat, P.; Nedelcu, G.; Walravens, W.; Maes, J.; Martins, J. C.; Van Driessche, I.; Kovalenko, M. V.Hens, Z. Highly Dynamic Ligand Binding and Light Absorption Coefficient of Cesium Lead Bromide Perovskite Nanocrystals. *ACS Nano* **2016,** *10* (2), 2071-2081.

(54) Dai, X.; Zhang, Z.; Jin, Y.; Niu, Y.; Cao, H.; Liang, X.; Chen, L.; Wang, J.Peng, X. Solution-processed, high-performance light-emitting diodes based on quantum dots. *Nature* **2014,** *515* (7525), 96-99.

(55) Taylor, J.; Brandbyge, M.Stokbro, K. Theory of Rectification in Tour Wires: The Role of Electrode Coupling. *Phys. Rev. Lett.* **2002,** *89* (13), 138301.

(56) Perdew, J. P.; Burke, K.Ernzerhof, M. Generalized Gradient Approximation Made Simple. *Phys. Rev. Lett.* **1996,** *77* (18), 3865-3868.

TOC graph

Highly stable and efficient dual-channel excitation (utilizing FRET) light-emitting diodes based on CaI_x/γ-$CsPbI_3$/CaI_2 seed/core/shell nanocrystals show a record external quantum efficiency of 25.3% and a brightness of 13626 cd/m^2.